Angewandte Chemie
Eine Zeitschrift der Gesellschaft Deutscher Chemiker

Supporting Information

High-Efficiency and Stable Li–CO_2 Battery Enabled by Carbon Nanotube/Carbon Nitride Heterostructured Photocathode

J. Li, K. Zhang, Y. Zhao, C. Wang, L. Wang, L. Wang, M. Liao, L. Ye, Y. Zhang, Y. Gao, B. Wang, H. Peng**

SUPPORTING INFORMATION

Table of Contents

SUPPORTING INFORMATION

Experimental section

Chemicals and materials. Lithium chips (99.9%, thickness: 0.4 mm, diameter: 16 mm) and lithium foil (99.9%, thickness: 30 μm) were obtained from China Energy Lithium Co., Ltd. Bis(trifluoromethane) sulfonimide (LiTFSI, trace metals basis, 99.95%), 1-ethyl-3-methylimidazolium tetrafluoroborate (EMIMBF$_4$, $C_6H_{11}BF_4N_2$, for electrochemistry, ≥ 99.0%), poly(vinylidene fluoride-co-hexafluoropropylene) (PVDF-HFP, M_w of 400000 and M_n of 130000), trimethylolpropane ethoxylate triacrylate (TMPET, average molecular weight of ~428), 2-hydroxy-2-methyl-1-phenyl-1-propanone (HMPP, $C_6H_5COC(CH_3)_2OH$, 97%), and sodium sulfate were purchased from Sigma Aldrich. Tetraglyme ($C_{10}H_{22}O_5$, 99%) and N-methyl pyrrolidone (99.9%) were purchased from Aladdin Reagent. Guanidine hydrochloride (CH_6ClN_3, 99.5%), poly(ethylene glycol) (Mn of 4000), and deuterium water (99.9%), nitric acid (65 vol%), and hydrochloric acid were purchased from Adamas Reagent. Highly conductive carbon nanotube (CNT) film (thickness: 10-15 μm, conductivity: 3-8×10^4 S·m^{-1}) was purchased from Chengdu Organic Chemicals Co. Ltd. Glass fiber separator (GF/A 1.6 μm) was purchased from Whatman Co. Ltd. The stainless-steel CR2032-type coin cells with mesh holes at the cathode sides were purchased from Shenzhen Kelude Company. The polymethylpentene film was purchased from Hangzhou Miaojie Daily Chemical Technology Co., Ltd.

CNT@C$_3$N$_4$ preparation. Firstly, the pristine CNT film was washed with acetone, ethanol, and deionized water in turn and dried at 80 ºC in a vacuum oven. Then, the dried film was transferred to 65 vol% nitric acid and reflux heated at 120 ºC for 3 h to improve hydrophilicity and remove impurities. Next, the hydrophilic CNT film was immersed into an aqueous solution containing 1.0 g·mL^{-1} guanidine hydrochloride and 2 mg·mL^{-1} poly(ethylene glycol) 4000 and heated at 80 ºC for 3 h. Then, the CNT film impregnated with the precursor solution was spread out in a crucible and dried at 120 ºC for 1 h in a vacuum oven. Finally, the crucible sealed with punched aluminum foil was heated at 600 ºC for 4 h with a heating rate of 2.3 ºC·min^{-1} and a cooling rate of 1 ºC·min^{-1} under an argon (99.99%, Shanghai Tomoe Gases Co., Ltd.) flow of 100 sccm in a quartz tube. The areal density of the pristine CNT film was about 0.4-0.5 mg·cm^{-2} and the loading mass C$_3$N$_4$ was about 0.1-0.2 mg·cm^{-2}. For control experiments, the powder samples of C$_3$N$_4$ 600 ºC and C$_3$N$_4$ 550 ºC were synthesized by directly calcining guanidine hydrochloride at 600 ºC and 550 ºC with the same heating and cooling rates under argon atmosphere. The physical mixture of CNT and C$_3$N$_4$ (CNT/C$_3$N$_4$) was prepared by dipping C$_3$N$_4$ 600 ºC ethanol dispersion on the CNT film with C$_3$N$_4$ loading mass of about 0.2 mg·cm^{-2}.

C$_3$N$_4$/Ti cathode preparation. In order to distinguish the discharge product carbon from the intrinsic CNT matrix in the heterostructured photocathode, a carbon-free C$_3$N$_4$/Ti mesh cathode was designed as an alternative photocathode to exclude the interference of CNT in the CNT@C$_3$N$_4$. To remove carbon impurities, the Ti mesh was washed soaked in 65 vol% nitric acid for 10 s, boiled in 3 M hydrochloric acid at 80 ºC for 3 h, and finally rinsed by deionized H$_2$O. The C$_3$N$_4$/Ti mesh cathodes were prepared by dipping C$_3$N$_4$ 600 ºC dispersion on the Ti mesh with C$_3$N$_4$ loading mass of about 0.2 mg·cm^{-2}.

Electrolyte preparation. Both electrolyte preparation and battery assembly were conducted in an argon-filled glove box with O$_2$ and H$_2$O contents below 1.0 ppm. First, a precursor solution of gel electrolyte was prepared by mixing Solution A, B, and C. Solution A was prepared by dissolving 0.359 g LiTFSI in 1.622 g EMIMBF$_4$. Solution B was prepared by dissolving 0.5 g PVDF-HFP in 2.0 g NMP. Solution C was obtained by adding a drop of HMPP to 2.000 g TMPET. Then, the well-mixed precursor solution was cast on a piece of glass fiber separator, followed by 365 nm ultraviolet irradiation for 10 s to produce the quasi-solid gel electrolyte. The glass fiber separator was utilized to avoid the short circuit of the battery. Similarly, the tetraglyme gel electrolyte was prepared by replacing the above Solution A with 1.0 M LiTFSI in tetraglyme.

Coin battery assembly. The coin battery was assembled by successively stacking a lithium chip anode, a gel electrolyte, and a CNT@C$_3$N$_4$ cathode in a top-holing CR2032 coin cell. A layer of transparent polymethylpentene film was attached to the outside of the cathode hole to prevent the entrance of moisture and the volatilization of liquid components in the electrolyte.

Fiber battery assembly. First, lithium foil was evenly wrapped around a copper wire as anode fiber. Next, this anode fiber was dipped into and taken out of the as-prepared precursor solution of gel electrolyte and exposed to 365 nm ultraviolet irradiation for 10 s. The above process was repeated at least three times. Finally, the CNT@C$_3$N$_4$ and polymethylpentene film were wrapped on the gel electrolyte to obtain the final fiber battery.

Electrochemical measurements. The galvanostatic electrochemical measurements were carried out on the LAND cycler (CT2001A, Wuhan LAND Ltd.). Cyclic voltammetry curves and Nyquist plots were collected by an electrochemical workstation (CHI660E, Shanghai Chenhua Ltd.). The assembled battery was transferred to a homemade gas-tight glass bottle (volume capacity: 500 mL). High-purity CO$_2$ (99.99%, Shanghai Tomoe Gases Co., Ltd.) was purged into the bottle with a flowing rate of 100 sccm. The electrochemical characterizations were started after keeping on open circuit for 3 h. The flowing rate was adjusted to 20 sccm during testing. The light

was provided by a solar simulator with AM 1.5 solar light (equipped with a 350 W Xenon lamp and an AM 1.5 filter-typical solar spectrum, Shanghai Lansheng Electronic Technology Co., Ltd.). The wavelength distribution of the light source was tested by a spectrophotometer (Photoresearch 271 PR-680). The power density was tested by a light power meter (CEL-NP2000, Beijing China Education Au-light Technology Co., Ltd.). The ionic conductivity of electrolyte was obtained from the electrochemical impedance spectroscopy with a bias voltage of 5 mV and a frequency range from 10^5 to 0.1 Hz in a homemade testing device with two parallel stainless-steel tablets (1 × 1 cm^2) in the cured gel electrolytes. The electrochemical stability of electrolyte was investigated by the linear sweep voltammetry measurement in a coin cell of Li chip/electrolyte/stainless-steel-tablet. For the electrochemical measurements at a low-temperature environment, the battery was submersed in a home-made transparent glass container filled with dry ice through which Xenon lamp illuminated directly on the battery cathode. Dry ice was continuously replenished to keep the testing temperature constant. Due to the thermal effect of Xenon lamp, the realistic ambient temperature of battery in the dry ice was approximately −60 °C, higher than the sublimation temperature of dry ice (–78.5 °C).

Photoelectrochemical measurements. All the following measurements were performed in an electrochemical workstation (CHI660E, Shanghai Chenhua Ltd.). The CNT and CNT@C_3N_4 film (1 × 2 cm^2) were used as analytical samples with a testing area of 1 cm^2 (1 × 1 cm^2). For the C_3N_4 sample, 10 mg C_3N_4 was dispersed into a mixed solution containing 500 μL ethanol, 500 μL ethylene glycol, and 80 μL 5 wt% Nafion solution by sonication. Then, 80 μL of the dispersion was spread on the conductive side of indium tin oxide glass (1 × 2 cm^2) and dried at 70 °C for 2 h in a vacuum oven. In a transparent quartz cell, the analytical sample, a platinum foil electrode, and a saturated calomel electrode were used as the working electrode, counter electrode, and reference electrode, respectively, with 0.5 M sodium sulfate aqueous solution as electrolyte. Photocurrent response curves were recorded at a bias voltage of 0.5 V, and electrochemical impedance spectra were collected with a bias voltage of 5 mV and a frequency range of 10^5-0.1 Hz.

Materials characterizations. For the morphology and structural characterizations of CNT@C_3N_4 cathodes, the batteries were discharged or/and recharged to 0.5 mAh·cm^{-2} at 0.02 mA·cm^{-2} in the light or dark. After electrochemical treatments, the batteries were transferred into an argon glove box and the cathodes were extracted out of batteries. The cathodes were rinsed in 1, 3-dioxolane to wash off the residual electrolyte salt and solvent and then dried by evaporation and stored in the glove box. All the characterizations were carried out on the sides of cathodes facing illumination. The morphologies were characterized by the field-emission scanning electron microscopy (FESEM, Zeiss Ultra-55, operated at 5 kV, sputter-coated with a layer of gold nanoparticles) with energy dispersive X-ray spectroscopy (EDS) element mapping and transmission electron microscopy (JEOL JEM-2100 LaB_6). The structures were characterized by X-ray diffraction spectroscopy (Bruker AXS D8 powder X-ray diffractometer, Cu Kα radiation, 40 kV, 40 mA), Fourier-transform infrared spectroscopy (Nicolet 6700, equipped with a diamond attenuated total reflectance accessory, GladiATR, PIKE Technologies), Raman spectroscopy (Horiba LabRAM HR Evolution Spectrometer, with a 638 nm laser excitation wavelength), electron paramagnetic resonance (Bruker EMX PLUS), and X-ray photoelectron spectroscopy (Thermo Scientific K-Alpha Al Kα, $h\upsilon$ = 1486.6 eV, 12 kV, 6 mA) at room temperature. All the binding energy values were referenced to the C 1s peak of carbon at 284.8 eV. The hydrophilicity of CNT with/without acid treatment was characterized by the contact angle testing instrument (OCA40, Dataphysics).

The optical properties and band structure of CNT@C_3N_4 were characterized by the ultraviolet-visible spectrophotometer (Perkin-Elmer Lambda 750), fluorescence spectroscopy (PTI QM 40), and ultraviolet photoelectron spectroscopy (Thermo Fisher, ESCALAB 250XI PHI5000 VersaProbe III, He I light, 21.2 eV). In the testing of ultraviolet photoelectron spectroscopy, the work function was measured with a bias voltage of –5 V, and no bias voltage was applied in the measurement of the valence band spectrum. The thermal stability of electrolytes was characterized by a thermal gravimetric analyzer (Mettler Toledo). 10 mg electrolyte was placed in an opened alumina crucible and heated from 25 to 500 °C at a rate of 10 °C·min^{-1} in nitrogen.

Nuclear magnetic resonance (NMR) spectra were used to examine the stability of the electrolytes. The NMR spectra were collected using a spectrometer (Bruker AVANCE III HD, 400 MHz) at room temperature. The batteries were discharged or/and recharged to 0.10 mAh·cm^{-2} at 0.10 mA·cm^{-2} for one or ten cycles in the light or dark. The gel electrolytes and cathodes were taken out of batteries, transferred into 1 mL deuterated H_2O, stood for 24 h, and then the extracted solution was transferred to the septa-sealed NMR tubes. Similarly, the as-prepared gel electrolyte was put into 1 mL deuterated H_2O and stood for 24 h as the pristine electrolyte sample. Typically, ^1H and ^{13}C NMR spectra of samples were tested for 64 and 256 scans, respectively. All the optical photographs were taken by a mobile phone (MI 9).

Gas chromatography measurement for the Li-CO_2 battery during charge. To analyze the gas products during charge, the battery was firstly discharged at 50 μA for 5 h in a home-made testing bottle. Next, the bottle was flushed with Ar to fully remove CO_2. Then, the gas product was collected and analyzed online continuously by a gas chromatograph (Ruimin Technologies, GC2060) with Ar as the carrier gas when the battery was charged at 50 μA. The gas chromatograph was equipped with a packed TDX-01 column, a packed 5A column and Porapak T column.

SUPPORTING INFORMATION

Band structure calculation. The band structure could be obtained combining ultraviolet photoelectron spectra and Tauc curve.[1,2] Firstly, the valence band was estimated to be at –1.42 eV (*vs. Fermi level*) from the ultraviolet photoelectron spectra by the linear intersection method, and the work function of C_3N_4 was calculated to be W = hν – 16.81 eV = 21.2 – 16.81 = 4.39 eV (*vs. vacuum*), corresponding to Fermi level of −4.39 *eV* (*vs. vacuum*). Then, the valence band edge was obtained as –5.81 eV (*vs. vacuum*). Based on the relationships among the vacuum level, the normal electrode potential *(NHE),* and the relative electrode potential [E(eV, *vs. vacuum*) = –eE (V, *vs. NHE*) – 4.44, E(V, *vs.* Li^+/Li) = E(V, *vs. NHE*) + 3.04], the valence band potential was calculated to be E_{VB} = 4.41 V (*vs.* Li^+/Li). With the bandgap (E_g) of 2.57 eV, the conduction band potential was at *ca.* 1.84 V (*vs.* Li^+/Li). Since the thermodynamic equilibrium potential of the Li-CO_2 battery (2.80 V) was between the conduction band and valence band of C_3N_4, the photogenerated electrons/holes at the cathodes could participate in the discharge/charge reactions of Li-CO_2 battery theoretically.

Calculation section

Density functional theory calculations. The density functional theory (DFT) calculations were performed using the Vienna Ab initio Simulation Package (VASP). The exchange-functional was treated using the Perdew–Burke–Ernzerhof (PBE) functional. The cut-off energy of the plane-wave basis was set at 450 eV. For the CNT/defective C_3N_4 model, the Monkhorst–Pack k-point mesh was set as 2 × 2 × 1. A force tolerance of 0.01 eV $Å^{-1}$ and an energy tolerance of 1.0×10^{-5} eV per atom were considered during the geometry optimization. A vacuum of 20 Å was used to eliminate interactions between periodic structures. DFT-D method of Grimme was used to treat the van der Waals interaction. A 2 × 2 C_3N_4 supercell with a removed pyridine N atom was adopted as the defective C_3N_4 monolayer for a moderate defect concentration. A graphene monolayer containing 72 carbon atoms was used for the simplified calculations. The heterostructure was modeled as a stable bilayer parallel graphene/defective C_3N_4 stacking structure. The interface adhesion energy was obtained according to the following formula, $E_{ad} = E_{complex} - E_{CNT} - E_{g\text{-}C3N4}$, where $E_{complex}$, E_{CNT}, and E_{C3N4} denoted the total energies of heterostructure complex, graphene monolayer, and C_3N_4 monolayer, respectively.

Finite difference time domain (FDTD) simulations. The FDTD simulations were performed using the *FDTD Solutions* (Lumerical). To predict the electric field distribution around CNT@C_3N_4, a geometric model of CNT@C_3N_4 was constructed with C_3N_4 layer (thickness: 10 nm) closely wrapped around CNT (diameter: 30 nm) in a vacuum medium through which the irradiating light transmitted. The enhancement in electric near-field over the cross-section was calculated in a domain of 90 × 90 nm^2 under an illuminated plane wave in the wavelength region from 300 to 800 nm. The perfectly matched layer condition and periodic boundary condition were chosen in the propagation and two transversal directions, respectively. The space was discretized with a resolution of 1 nm.

Results and discussion

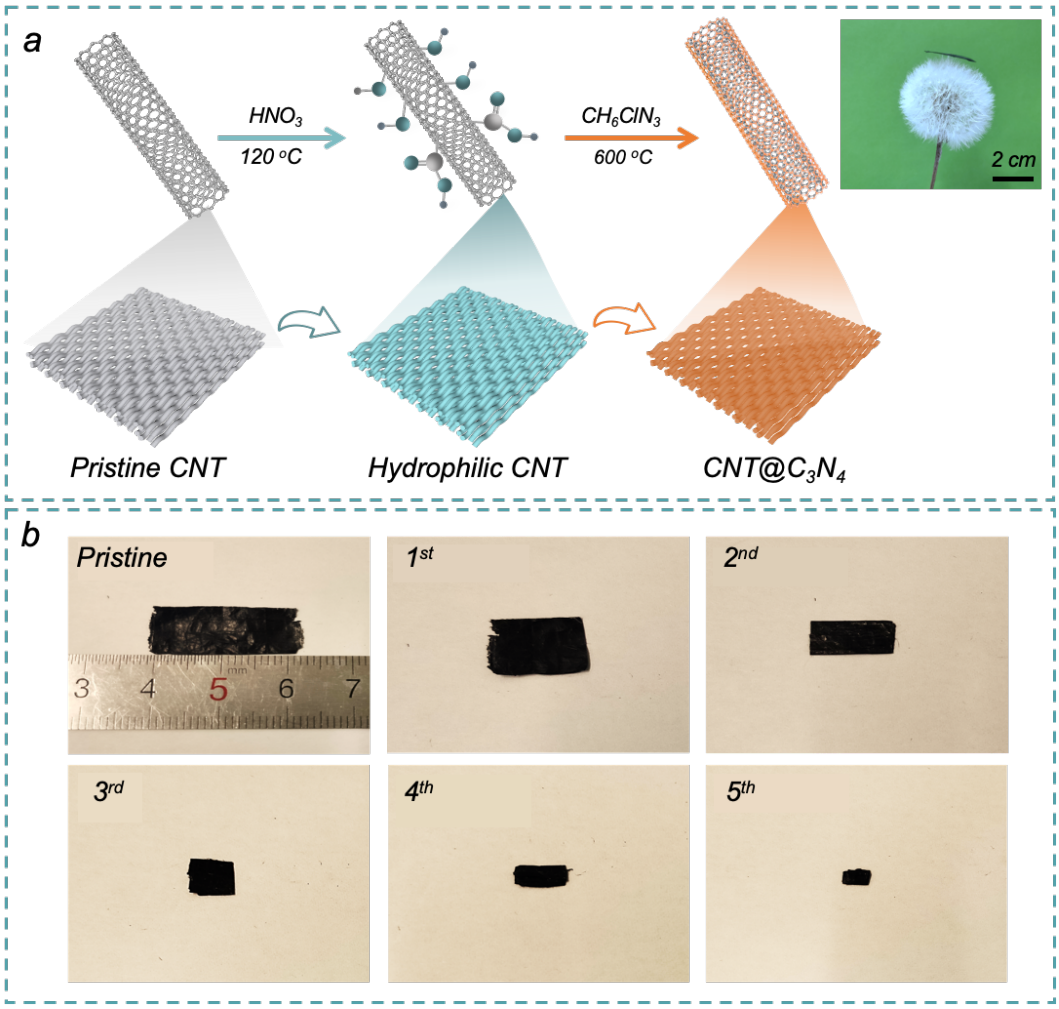

Figure S1. (**a**) Preparation of CNT@C_3N_4 heterostructured photocathode. The inset image is a piece of CNT@C_3N_4 film lying at the top of a dandelion. (**b**) Folding process of a piece of CNT@C_3N_4 film.

The above results demonstrated the light weight and flexibility of CNT@C_3N_4 film.

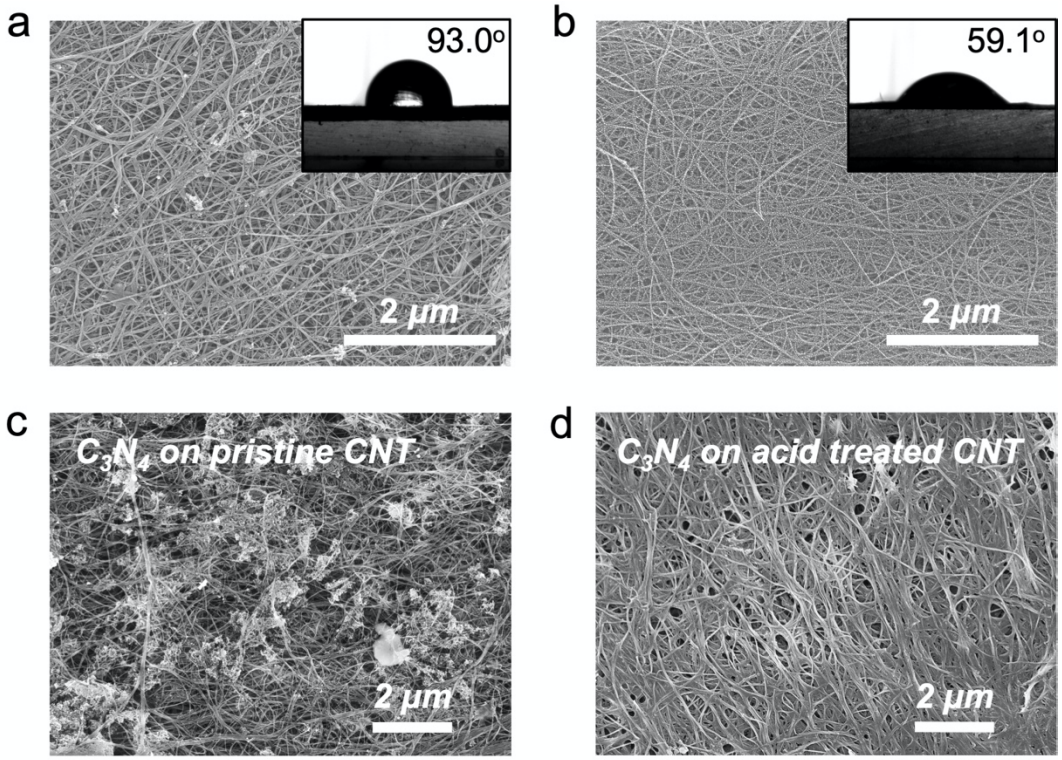

Figure S2. Scanning electron microscopy images of (**a**) pristine CNT, (**b**) acid treated CNT, (**c**) C_3N_4 growing on pristine CNT and (**d**) acid treated CNT. The insets in (**a**) and (**b**) indicate the contact angles between a water droplet and CNT with or without acid treatment.

The acid treatment process enhanced the hydrophilicity of CNT, afford good contact with aqueous precursor solution, and thus enable the uniform growth of C_3N_4 on CNT surface. Therefore, this step was vital to the construction of the heterostructured photocathode.

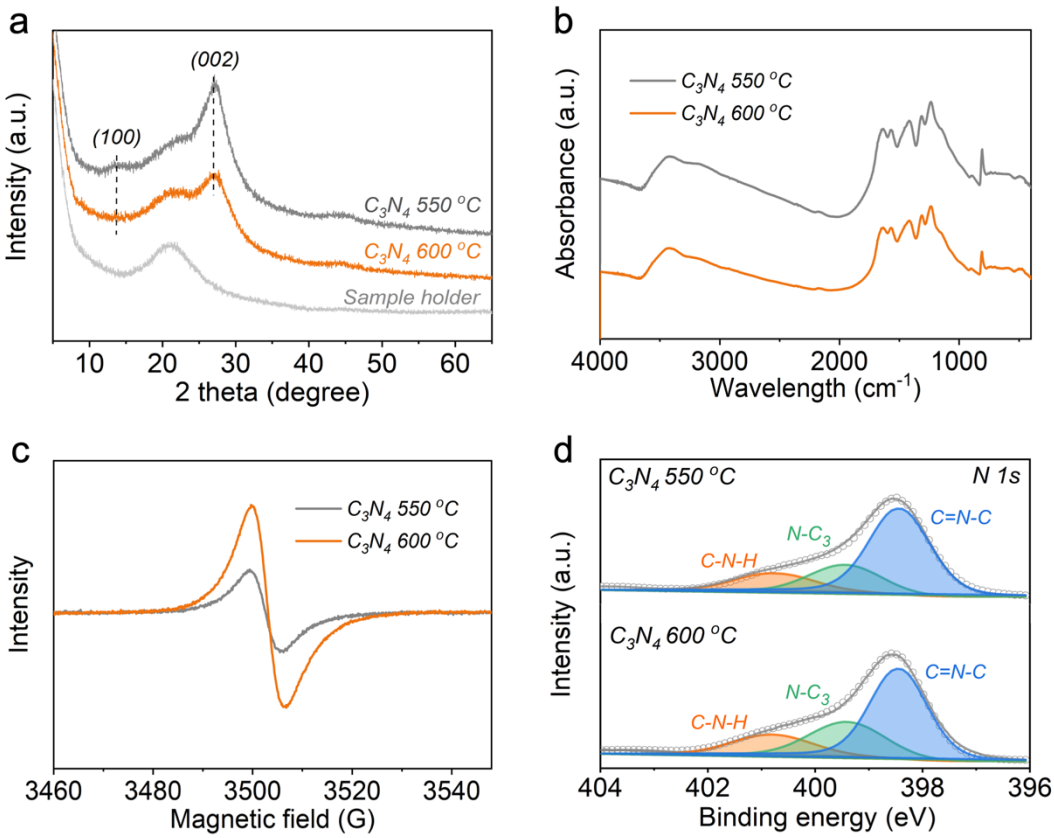

Figure S3. Structural characterizations of C_3N_4 synthesized at 550 °C (typical synthesis temperature) and 600 °C (materials in this study). (**a**) X-ray diffraction spectra. (**b**) Fourier-transform infrared absorption spectra. (**c**) Electron paramagnetic resonance spectra. (**d**) N 1s X-ray photoelectron spectra.

C_3N_4 550 °C showed two typical X-ray diffraction peaks at 13° and 27° (**Figure S3a**), assigned to the (100) and (002) planes of C_3N_4 and corresponding to the in-plane packing structure of tri-s-triazine units and interlayer stacking of the conjugated aromatic system. In comparison, C_3N_4 600 °C showed much weaker intensities in the two peaks, suggesting the loss of ordered structure within C_3N_4. Both the two materials presented similar molecular structure including the N-H groups (3000-3500 cm^{-1}), C-N heterocycles (1200-1800 cm^{-1}), triazine groups (800-810 cm^{-1}) (**Figure S3b**). Notably, the higher electron paramagnetic resonance intensity at g=2.003 implied the existence of more unpaired electrons on the carbon atoms and nitrogen defects in C_3N_4 600 °C than C_3N_4 550 °C (**Figure S3c**). The ratio of C=N-C (two-coordinated N) and N-C_3 (three-coordinated N) in the N 1s spectra dropped to 2.18 (C_3N_4 600 °C) from 2.96 (C_3N_4 550 °C) (**Figure S3d**), indicating that the nitrogen defects could be located at C=N-C sites.

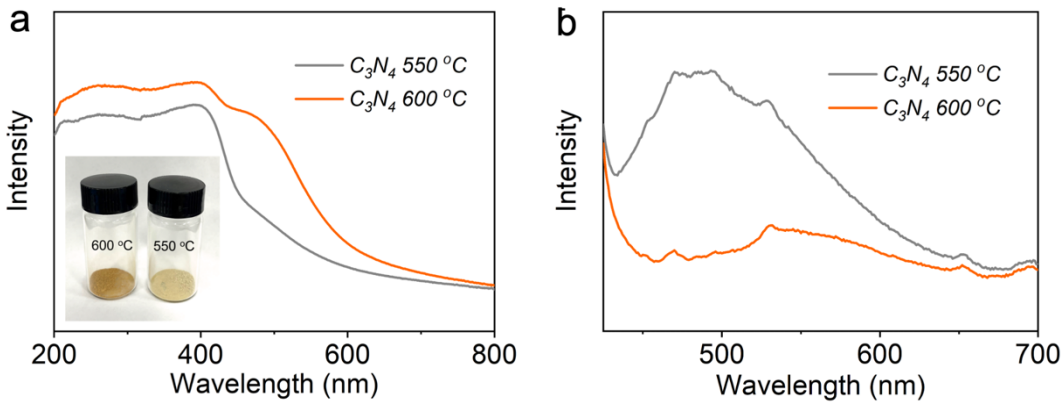

Figure S4. (**a**) Ultraviolet-visible absorption spectra and (**b**) steady-state photoluminescence emission spectra of C_3N_4 synthesized at 550 °C (typical synthesis temperature) and 600 °C (materials in this study). The inset image is a photo of C_3N_4 materials synthesized at 550 °C and 600 °C.

C_3N_4 600 °C took on a darker yellow than C_3N_4 550 °C, corresponding to the extensive visible-light absorption (**Figure S4a**). In sharp contrast with the strong fluorescence emission peak centered at 470 cm^{-1} for C_3N_4 550 °C, C_3N_4 600 °C showed a much-lowered fluorescence emission peak (**Figure S4b**), implying the promoted separation of photogenerated charge carriers in C_3N_4 600 °C.

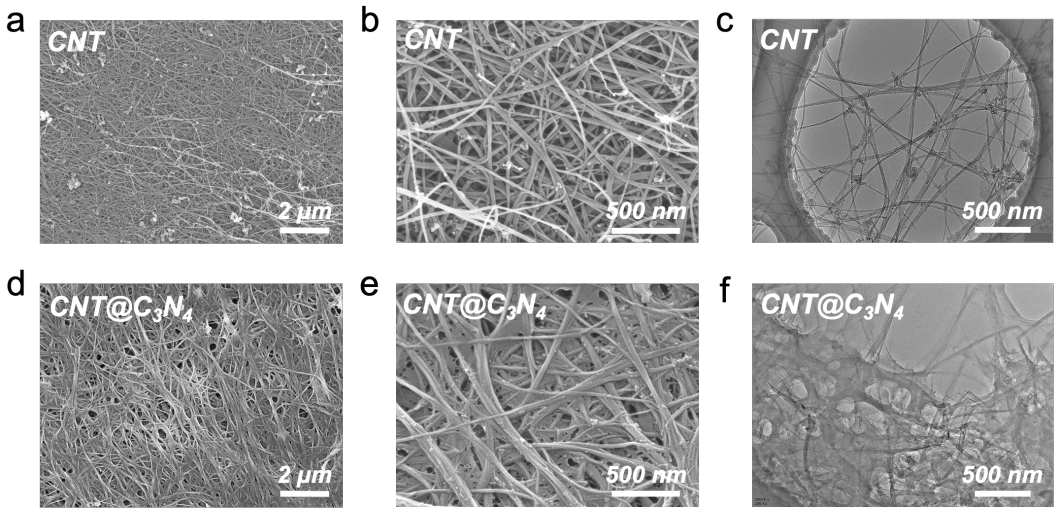

Figure S5. Scanning electron microscopy and transmission electron microscopy images of (**a-c**) CNT and (**d-f**) CNT@C_3N_4.

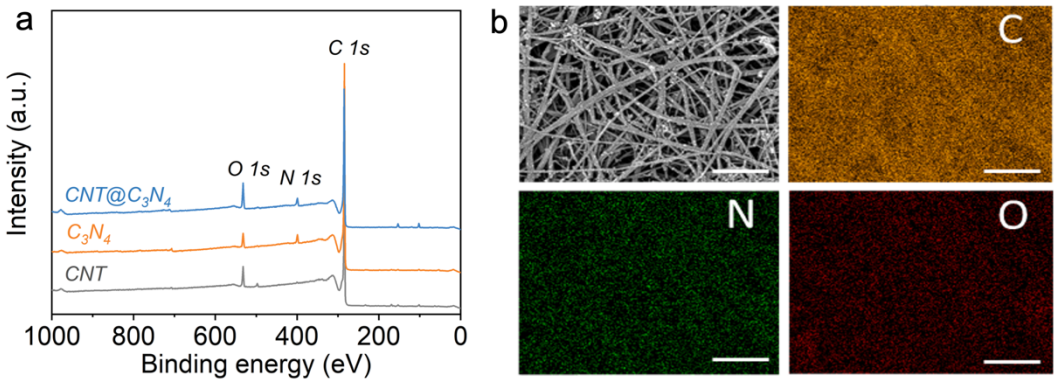

Figure S6. (**a**) X-ray photoelectron survey spectra of CNT, C_3N_4, and CNT@C_3N_4. (**b**) Scanning electron microscopy and energy-dispersive X-ray spectra elemental mapping images of CNT@C_3N_4. Scale bar, 1 μm.

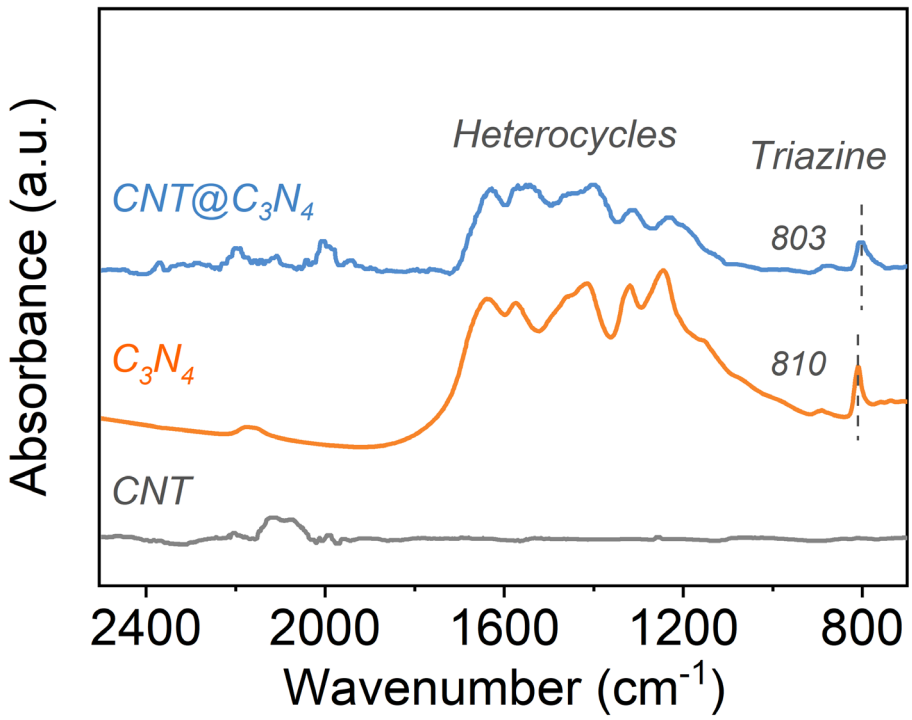

Figure S7. Fourier-transform infrared absorption spectra of CNT, C_3N_4, and CNT@C_3N_4.

The characteristic absorption peaks of the stretching and breathing patterns of C-N heterocycles (between 1200 and 1800 cm^{-1}) and the out-of-plane bending vibration of triazine ring units (800-810 cm^{-1}) appeared in the spectrum of CNT@C_3N_4, indicating the successful deposition of C_3N_4 on the CNT film.[3] The triazine units of CNT@C_3N_4 was shifted to 803 from 810 cm^{-1} of C_3N_4, indicating the presence of interaction between CNT and C_3N_4.

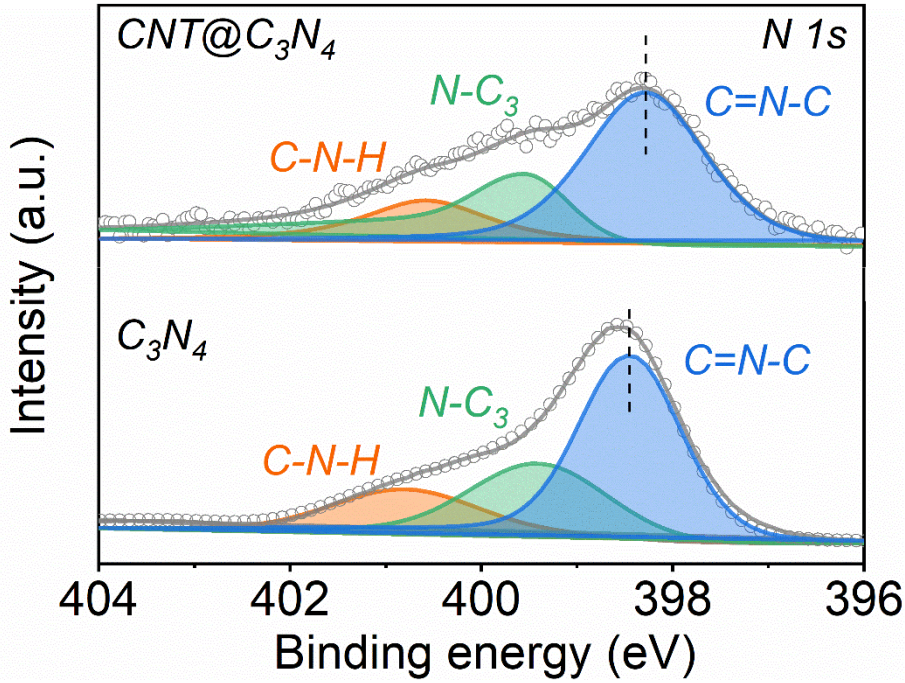

Figure S8. N 1s X-ray photoelectron spectra of C_3N_4 and CNT@C_3N_4.

The C=N-C peak of CNT@C_3N_4 demonstrated negative shift compared with that of C_3N_4, implying increased electron density on N atoms of the C=N-C units for CNT@C_3N_4. This could be caused by the electron transfer from CNT to C_3N_4.

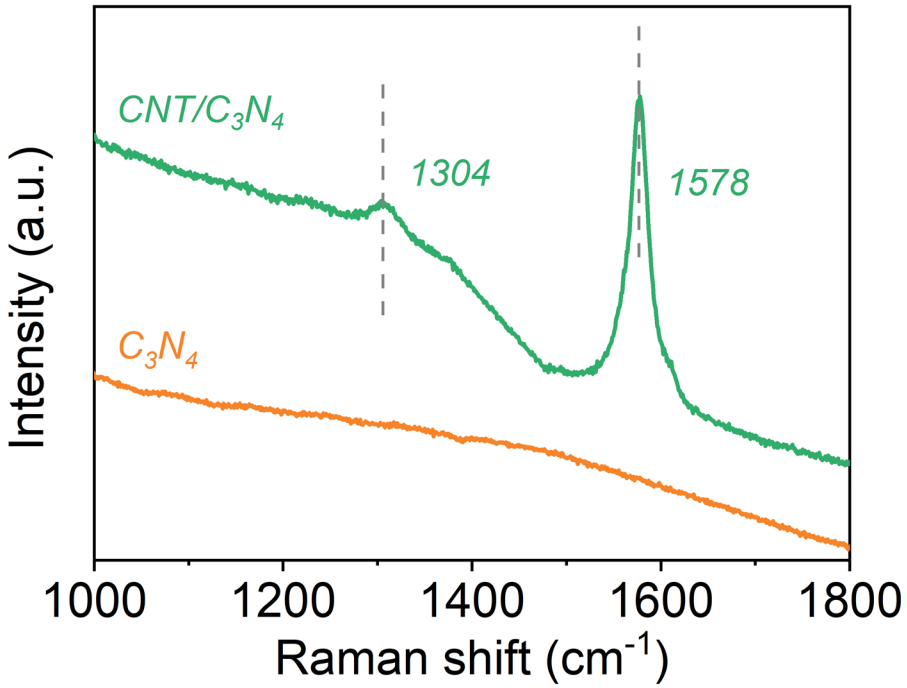

Figure S9. Raman spectra of C_3N_4 and CNT/C_3N_4 (physical mixture of CNT and C_3N_4).

No characteristic peak appeared in the Raman spectrum of C_3N_4 due to its poor crystallinity and intensive photoluminescence. For the CNT/C_3N_4, the obvious D and G bands were attributed to the CNT and the intensive photoluminescence effect implied serious recombination of photo-excited carriers of C_3N_4, due to the poor interfacial charge transfer between the physically mixed C_3N_4 and CNT.

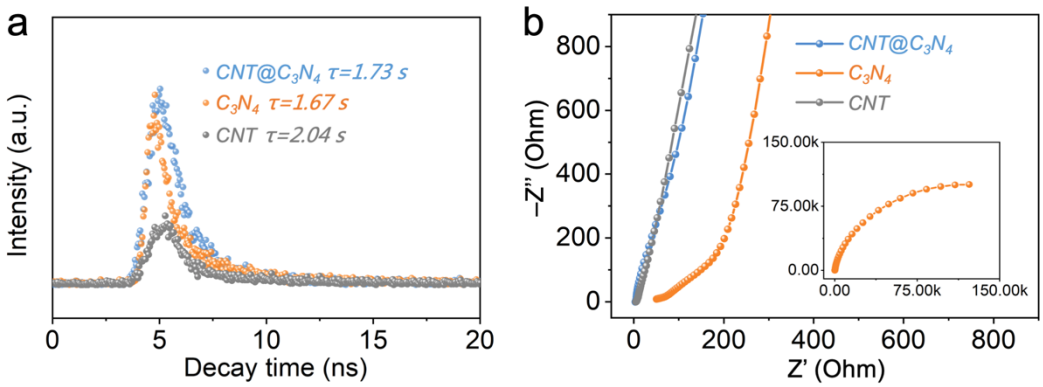

Figure S10. (**a**) Time-resolved transient photoluminescence decay spectra of CNT, C_3N_4, and CNT@C_3N_4. (**b**) Nyquist plots of CNT, C_3N_4, and CNT@C_3N_4.

The average fluorescent lifetime of CNT@C_3N_4 was longer than that of C_3N_4, demonstrating enhanced interfacial charge transfer between CNT and C_3N_4.

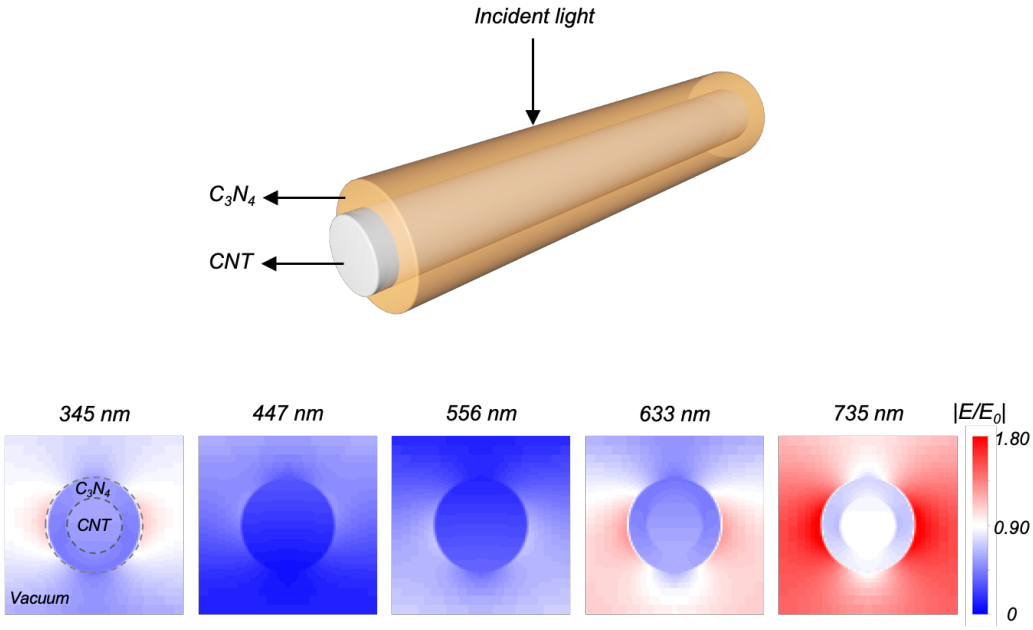

Figure S11. Finite difference time domain (FDTD) simulations of CNT@C_3N_4. Geometric model of CNT@C_3N_4 (top) and simulated electric field distribution around CNT@C_3N_4 at the representative wavelengths of 345, 467, 556, 633, and 735 nm in a square domain of 90 × 90 nm^2 (bottom).

According to the localized surface plasmon resonance effect, there is strong electric near-field enhancement around metal-semiconductor heterojunctions under the excitation of the incident light, owing to the differences in the optical properties of metal, semiconductor, and reactant.[6] The above results showed the enhanced electric near-field intensities around CNT@C_3N_4 under illumination, suggesting good spectral responsiveness of the CNT@C_3N_4 within the ultraviolet-visible wavelength range. This increase in electric near-field intensity would promote the formation of charge carriers and enhance the catalytic activity of photocathode. E_0 and E represent the intensities of the incident and localized electric field, respectively.

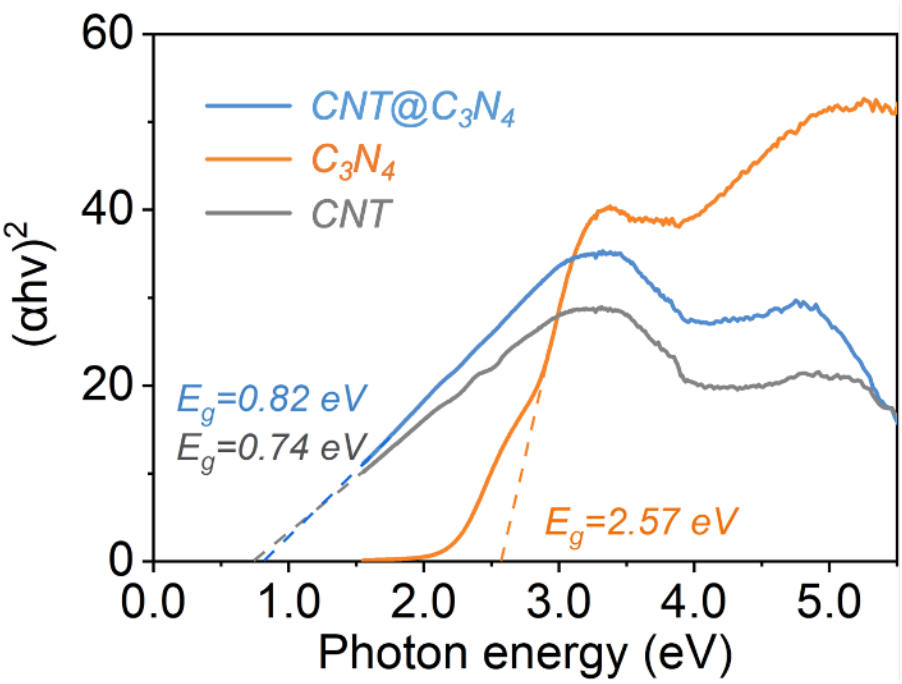

Figure S12. Tauc curves of CNT, C_3N_4, and CNT@C_3N_4. The E_g of C_3N_4 is measured to be 2.57 eV by measuring the X-axis intercept of an extrapolated line from the linear regime of the curve.

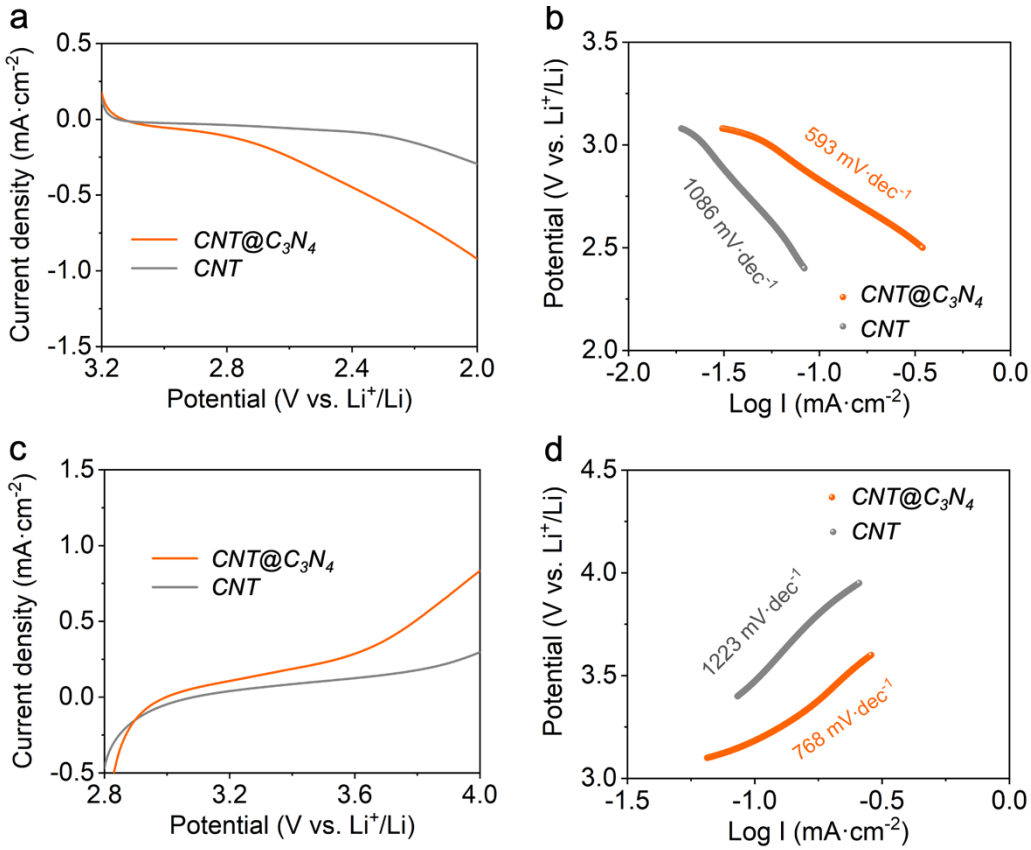

Figure S13. Linear sweep voltammetry and Tafel curves of CNT and CNT@C_3N_4 cathodes operated in the Li-CO_2 batteries under illumination.

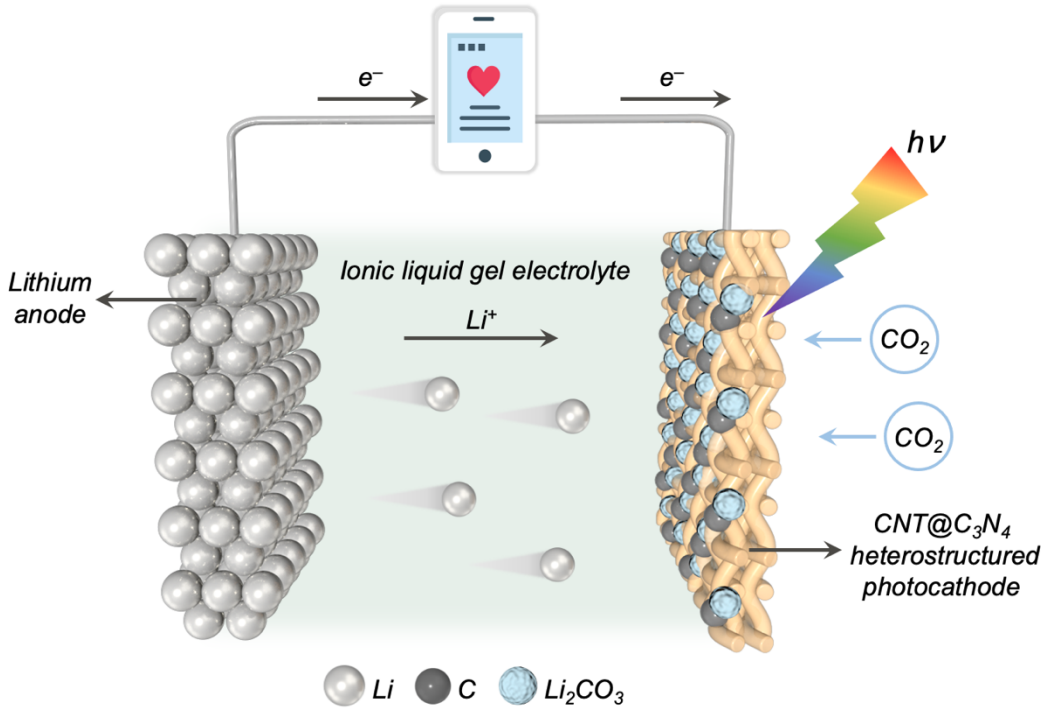

Figure S14. Schematic illustration of the light-assisted Li-CO_2 battery consisting of a CNT@C_3N_4 heterostructured photocathode, a metallic lithium anode, and an ionic liquid gel electrolyte.

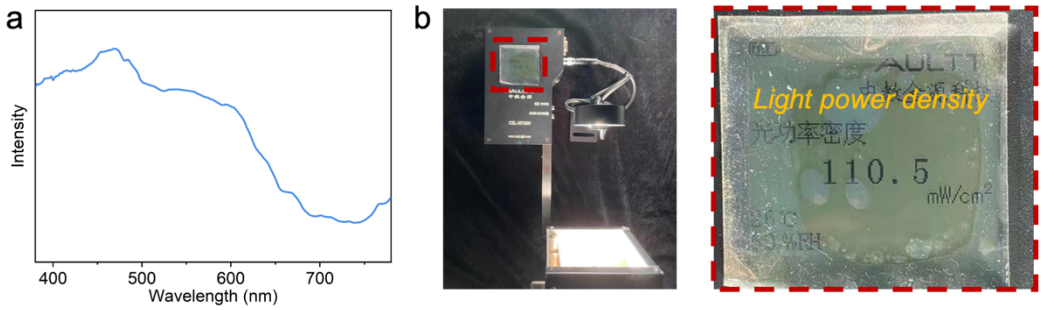

Figure S15. (**a**) Wavelength distribution and (**b**) power density of the Xenon lamp used in this research.

The light source presented a wavelength distribution from 380 to 780 nm with a power density of about 110 mW·cm^{-2}.

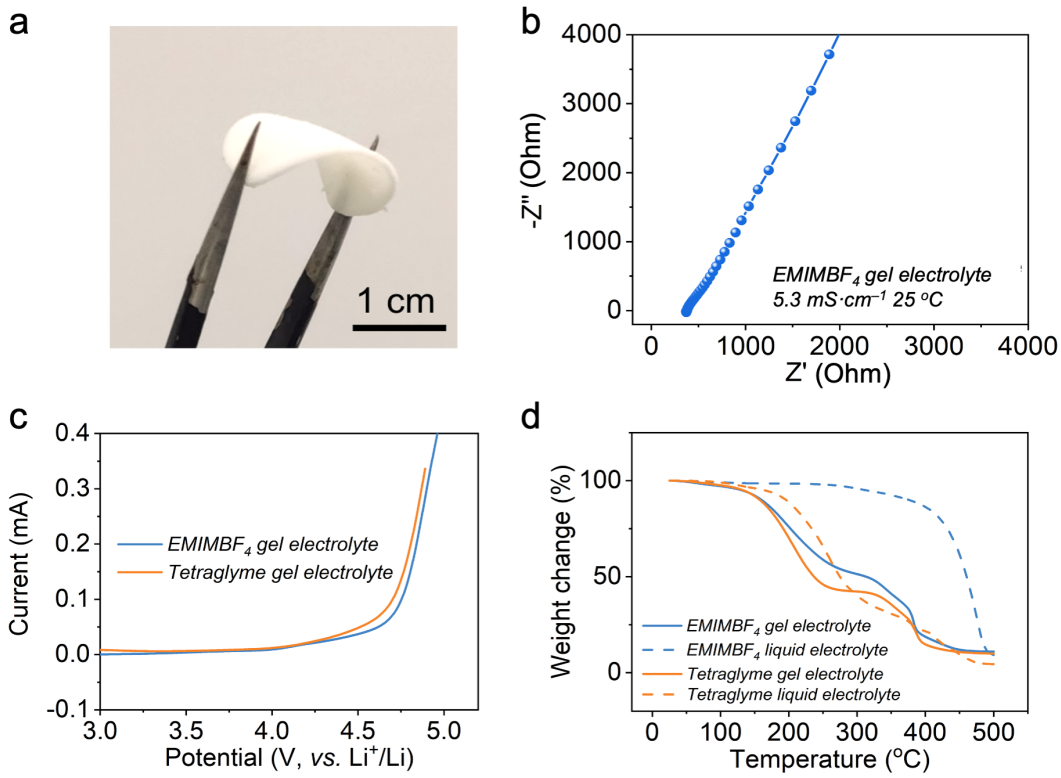

Figure S16. Characterizations of gel electrolyte. (**a**) A photo of a piece of gel electrolyte under bending deformation. (**b**) Nyquist plot of $EMIMBF_4$ gel electrolyte. (**c**) Linear sweep voltammetry curves of $EMIMBF_4$ and tetraglyme gel electrolytes. (**d**) Thermogravimetric analysis curves of $EMIMBF_4$ and tetraglyme based electrolytes.

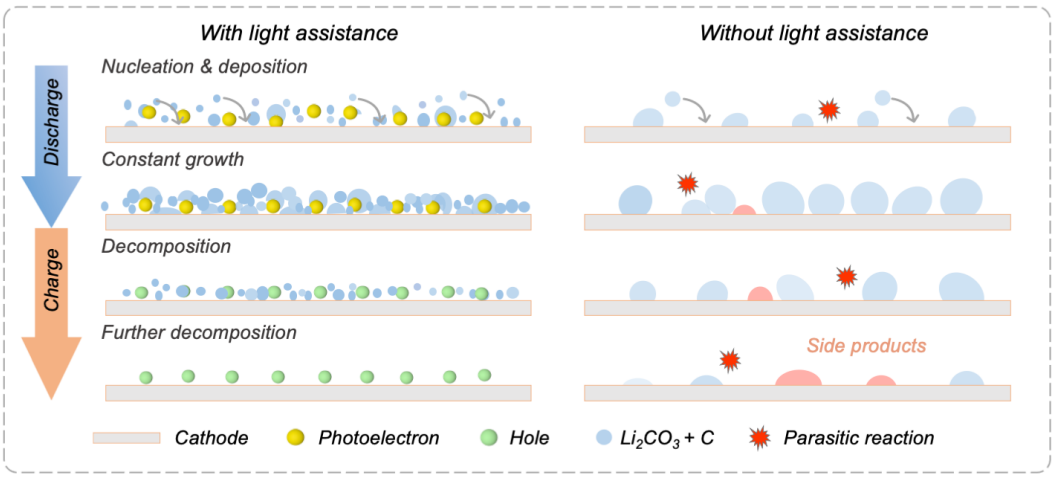

Figure S17. Proposed formation and decomposition pathways of discharge products at the CNT@C_3N_4 photocathodes under illumination (left) and in the dark (right).

During discharge, the cathode in the light presents favorable electronic structure to adsorb CO_2 and provides abundant nucleation sites for discharge product deposition than that in the dark. This results in the formation of more small particles in the light, in contrast with fewer large particles in the dark. During charge, the holes boost the decomposition of discharge products at a much lower charge voltage and inhibit the degradations of electrolyte and carbon-based cathode.

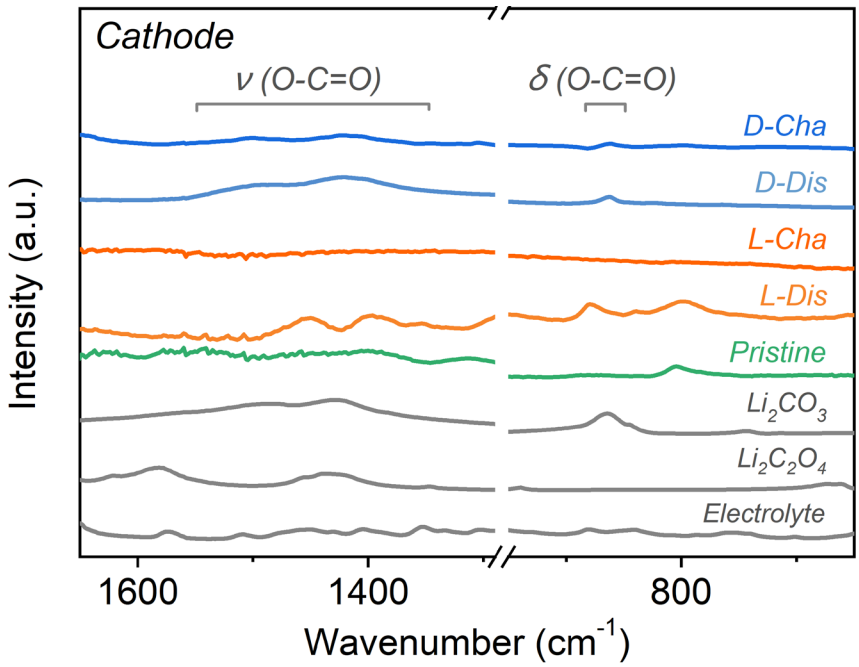

Figure S18. Fourier-transform infrared absorption spectra of the CNT@C_3N_4 heterostructured cathodes at different discharged/charged states in the light or dark. *L-Dis*, *L-Cha*, *D-Dis*, and *D-Cha* represent the batteries were discharged/charged in the light or dark.

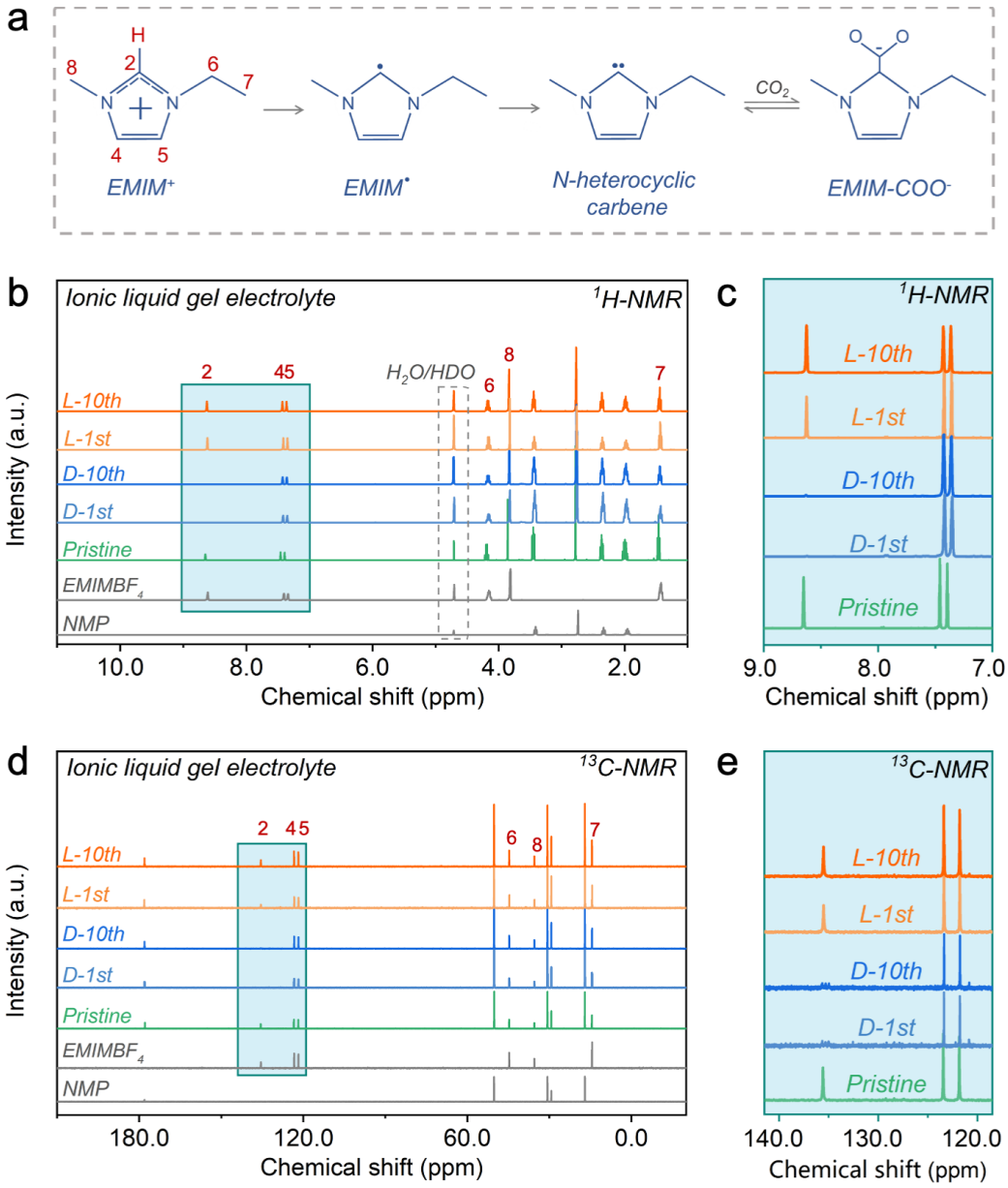

Figure S19. Stability analysis of the electrolytes in the light or dark. (**a**) Proposed decomposition pathway of $EMIMBF_4$. (**b, c**) ^{1}H and (**d, e**) ^{13}C NMR spectra of the deuterium water-extracted electrolytes from the cycled batteries in the light and dark.

There was no noticeable change in the position and intensity of the peaks corresponding to major electrolyte components, possible decomposition components, and moisture for the electrolytes in the light, proving the stability of electrolyte in the light. In contrast, the signals corresponding to the 2-position hydrogen (8.6 ppm in the ^{1}H NMR spectra) and carbon atom (135.5 ppm in the ^{13}C NMR spectra) of $EMIMBF_4$ were missing for the cycled electrolytes in the dark.[7] It is probably due to the abstraction of the most active α-hydrogen atoms on the imidazole rings of $EMIMBF_4$ molecules at the high polarized voltages,[8–10] with the generated N-heterocyclic carbene molecules being stabilized by the adhering alkyl groups or CO_2 molecules dissolved in the electrolyte.[11]

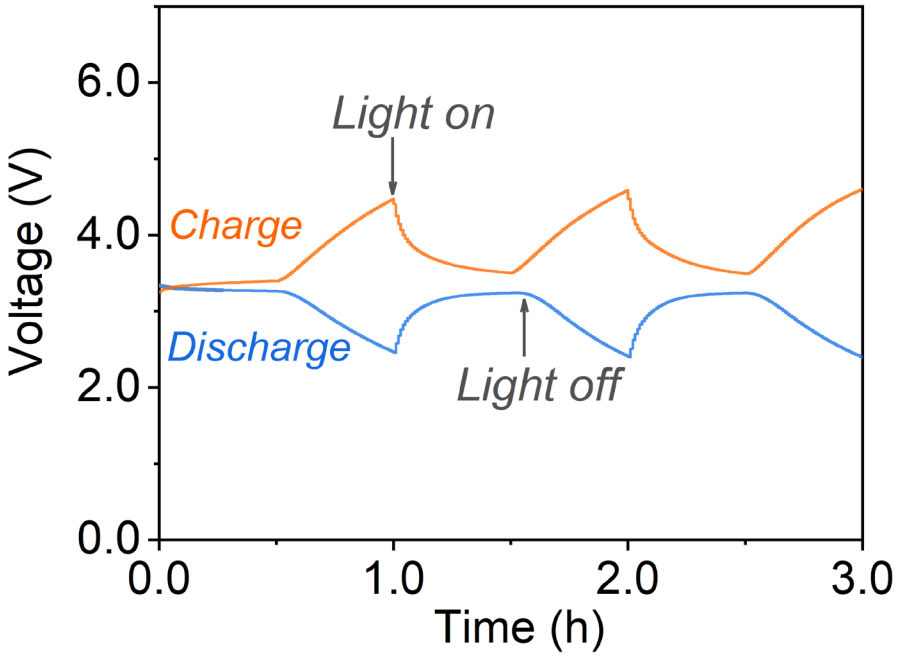

Figure S20. Discharge/charge curves responding to the intermittent light on/off with a current density of 0.02 mA·cm^{-2}.

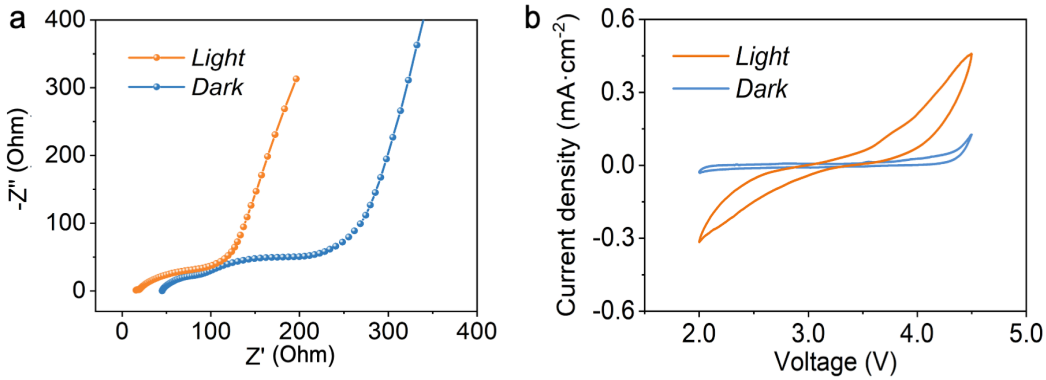

Figure S21. (**a**) Nyquist plots and (**b**) cyclic voltammetry curves of the Li-CO_2 batteries in the light and dark conditions.

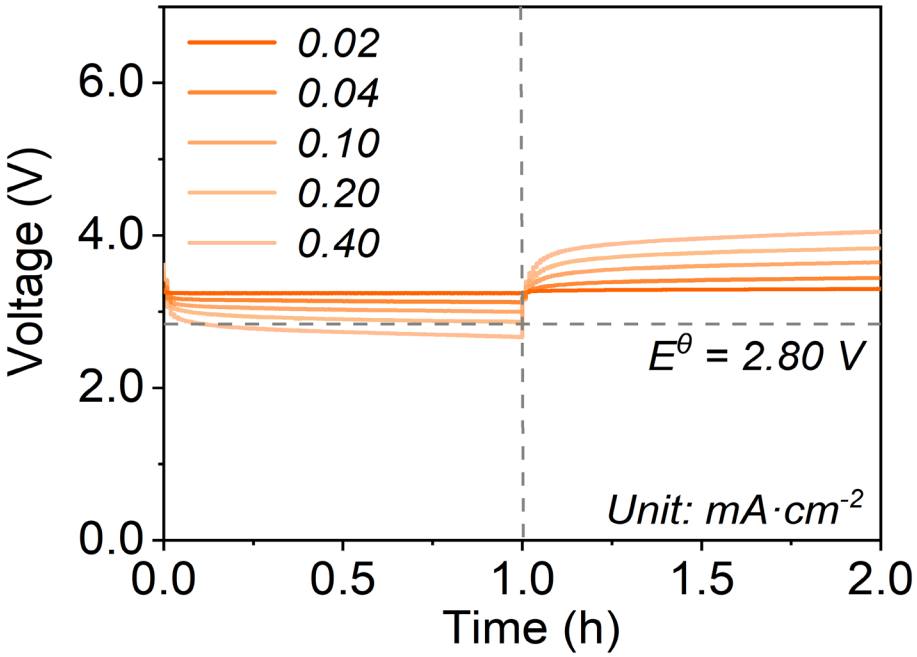

Figure S22. Discharge/charge curves of the Li-CO_2 batteries at varied current densities in the light.

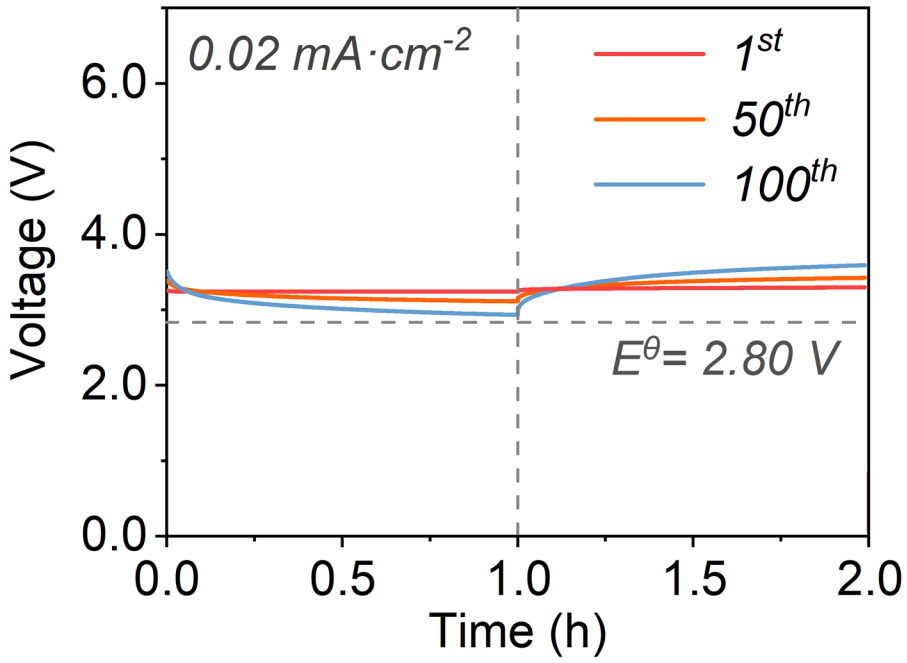

Figure S23. Discharge/charge curves of the Li-CO_2 battery at selected cycles in the light.

The discharge voltages were always higher than the thermodynamic equilibrium potential of 2.80 V, demonstrating superior CO_2 reduction kinetics at the heterostructured photocathode. The stable discharge/charge voltages upon cycling implied the high cycling stability of battery.

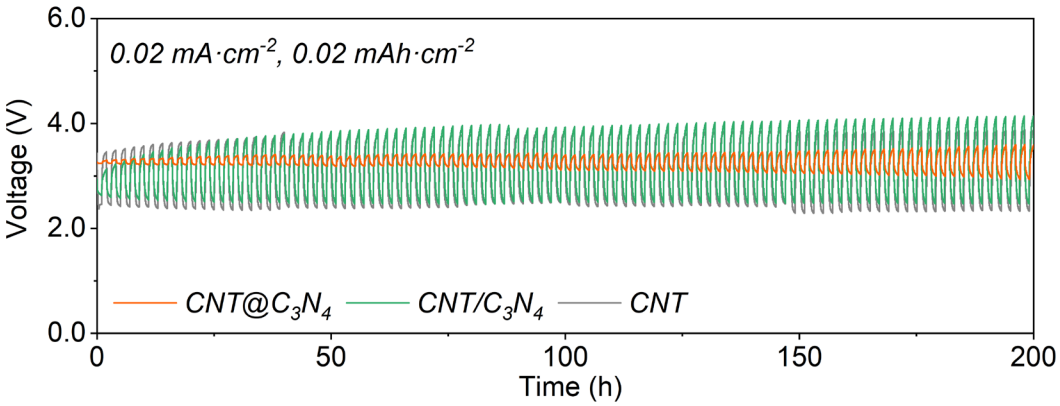

Figure S24. Cycling profiles of the Li-CO_2 batteries based on CNT@C_3N_4, CNT/C_3N_4 and CNT cathodes in the light.

Notably, CNT@C_3N_4 showed much smaller polarization gaps than other two counterparts upon cycling. The physical mixture of CNT and C_3N_4 (CNT/C_3N_4) presented a similar voltage evolution trend to the bare CNT probably due to the terrible interfacial charge transfer between C_3N_4 and CNT and the serious carrier recombination of C_3N_4.

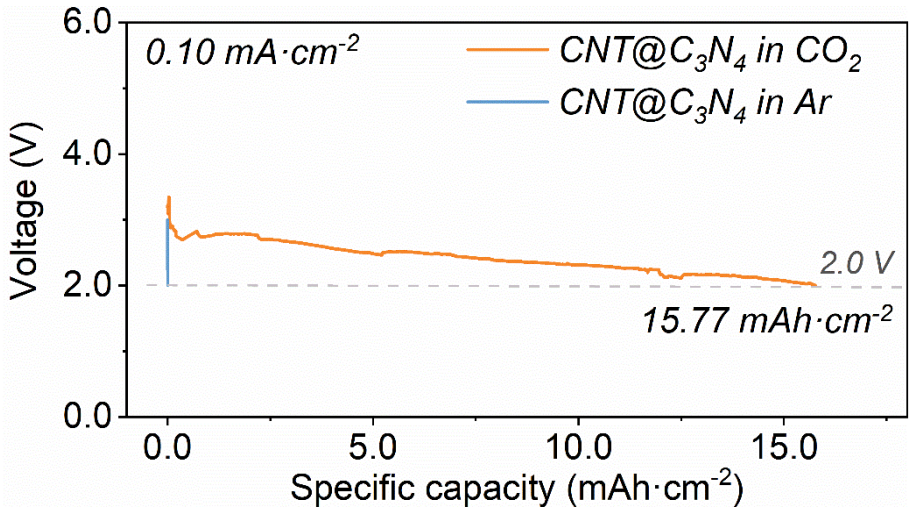

Figure S25. Deep discharge curves with a cut-off voltage of 2.0 V at 0.10 mA·cm^{-2} in CO_2 or Ar in the light.

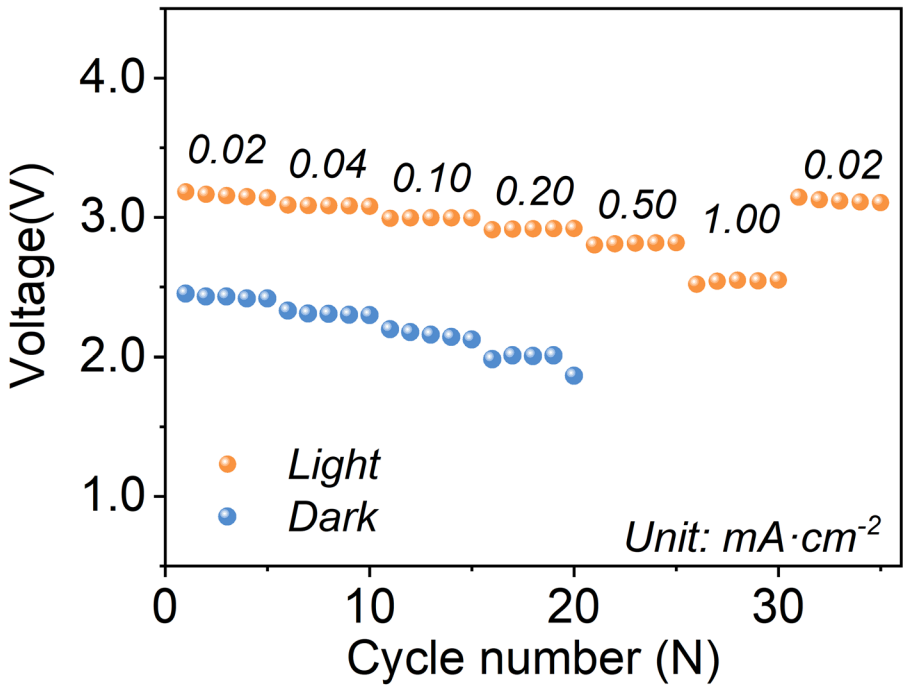

Figure S26. Rate cycling curves of the Li-CO_2 batteries in the light and dark.

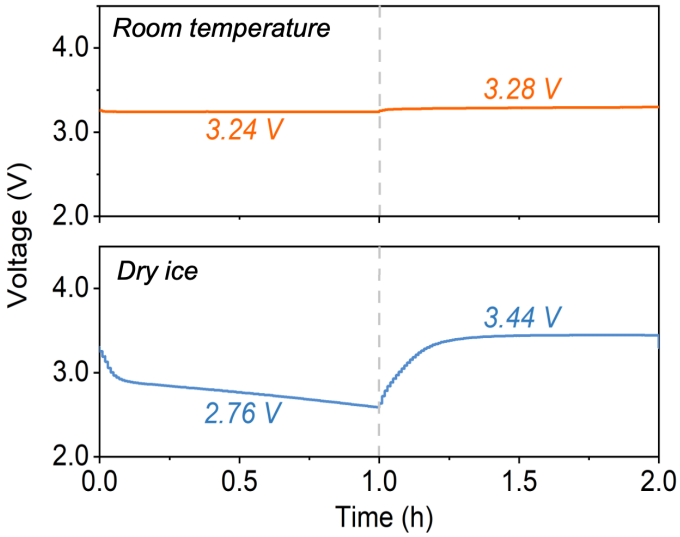

Figure S27. Discharge/charge curves of the Li-CO_2 batteries with a current density of 0.02 mA·cm^{-2} at room temperature or low temperature provided by dry ice.

Note that the realistic environment temperature of battery was around −60 °C due to the thermal effect of Xenon lamp.

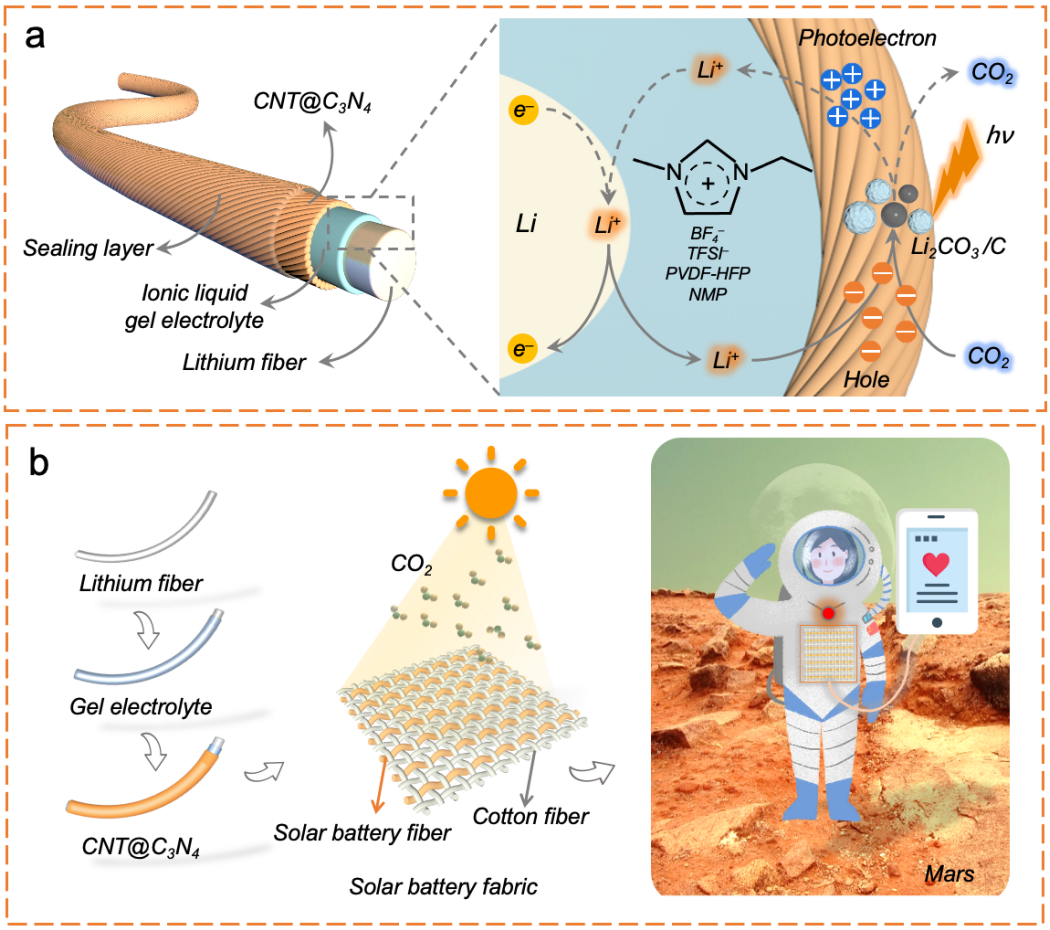

Figure S28. Schematic illustration of (**a**) a Li-CO_2 fiber battery and (**b**) a solar battery fabric woven with fiber Li-CO_2 batteries and possible application.

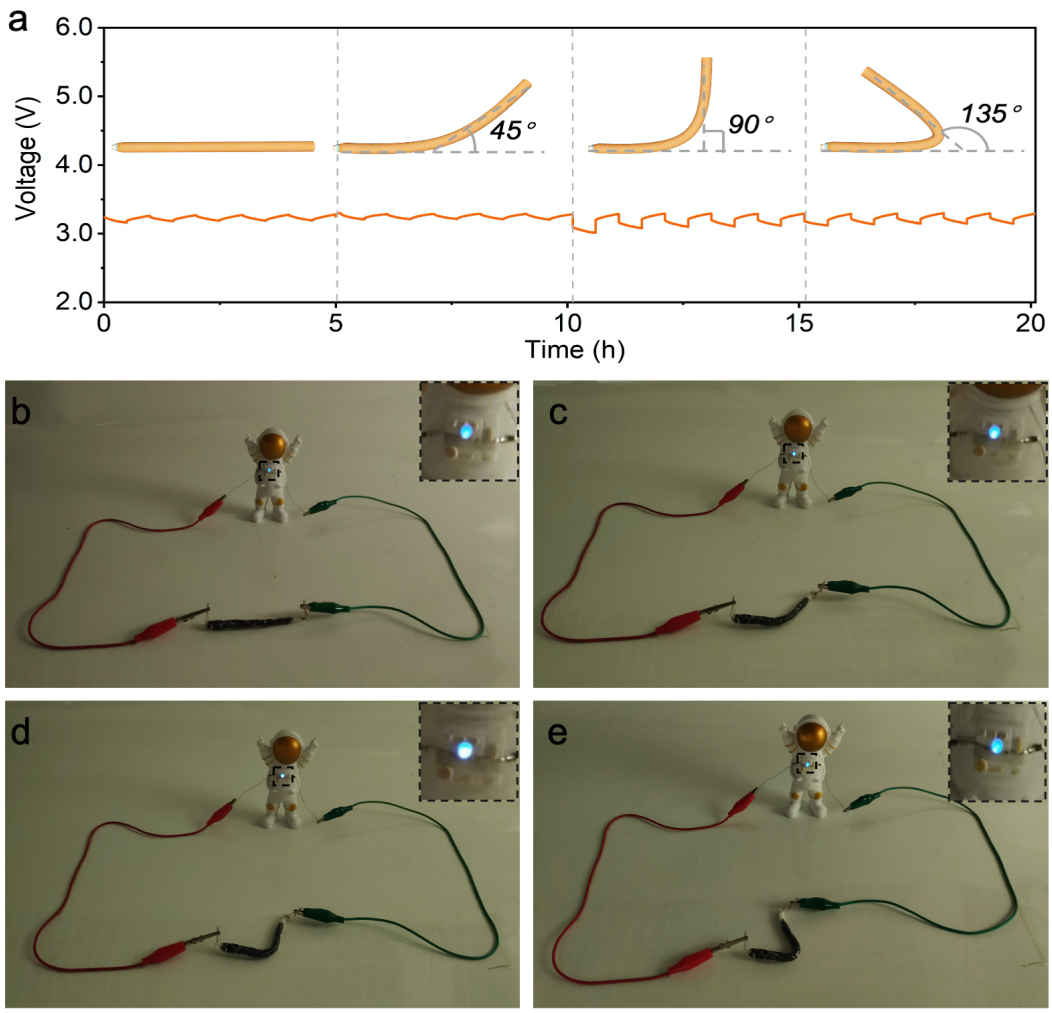

Figure S29. Application demonstration of fiber Li-CO_2 battery. (**a**) Discharge/charge curves a flexible fiber Li-CO_2 battery at different bending states in the light. (**b-e**) The fiber battery powering a blue light-emitting diode on an astronaut model.

SUPPORTING INFORMATION

Table S1. Comparison with some representative Li-CO_2 batteries.

Cathodes	Current density ($mA \cdot cm^{-2}$)	Cut-off capacity ($mAh \cdot cm^{-2}$)	1st voltage hysteresis (V)	1st round-trip efficiency	Cycling stability	Areal capacity ($mAh \cdot cm^{-2}$)	Ref.
$CNT@C_3N_4$ (Light-assisted)	**0.02**	**0.02**	**0.04**	**98.8%**	**86.1%, 100th**	**/**	**This work**
	0.10	**0.10**	**0.36**	**89.0%**	**67.5%, 100th**	**15.77**	
Cu_2O/CNT (Light-assisted)	0.04	0.40	~0.2	~90%	~86%, 50th	/	[12]
In_2S_3@CNT/SS (Light-assisted)	0.01	0.01	0.06	98.1%	~80%, 24th	/	[13]
SiC/RGO (Light-assisted)	0.01	0.01	0.51	84.4%	~70%, 80th	3.25	[14]
Ir NSs-CNFs	0.06	0.03	~0.9	~75%	~70%, 50th	2.54	[15]
CC@Mo_2C	0.02	0.10	0.65	~80%	~72%, 20th	3.42	[16]
CNT	0.02	0.40	1.65	~62%	~58%, 60th	3.41	[17]
Fe-ISA/N, S-HG	0.21	0.21	1.75	~60%	~57%, 50th	4.87	[18]
ZnS QDs/N-rGO	0.08	0.20	~1.5	~65%	65%, 50th	2.06	[19]
B, N-hG	0.03	0.39	~1.75	~60%	~58%, 50th	4.81	[20]
3D NCNT/G	0.04	0.40	1.13	71%	~69%, 50th	6.13	[21]

References

[1] Q. Lv, Z. Zhu, S. Zhao, L. Wang, Q. Zhao, F. Li, L. A. Archer, J. Chen, *J. Am. Chem. Soc.* **2020**, *143*, 1941-1947.
[2] J. C. Wang, H. C. Yao, Z. Y. Fan, L. Zhang, J. S. Wang, S. Q. Zang, Z. J. Li, *ACS Appl. Mater. Interfaces* **2016**, *8*, 3765-3775.
[3] K. Xiao, L. Chen, R. Yan, M. Oschatz, L. Jiang, M. Antonietti, *Angew. Chem. Int. Ed.* **2020**, *59*, 9067-9073.
[4] D. Zhao, C. Dong, B. Wang, C. Chen, Y. Huang, Z. Diao, *Adv. Mater.* **2019**, *31*, 1903545.
[5] G. Peng, J. Wu, M. Wang, J. Niklas, H. Zhou, C. Liu, *Nano Lett.* **2020**, 20, 2879−2885
[6] K. Awazu, M. Fujimaki, C. Rockstuhl, J. Tominaga, H. Murakami, Y. Ohki, N. Yoshida, T. Watanabe, *J. Am. Chem. Soc.* **2008**, *130*, 1676-1680.
[7] B. A. Marekha, O. N. Kalugin, M. Bria, A. Idrissi, *Phys. Chem. Chem. Phys.* **2015**, *17*, 23183-23194.
[8] P. A. Gokturk, U. Salzner, L. Nyulászi, B. Ulgut, C. Kocabas, S. Suzer, *Electrochim. Acta* **2017**, *234*, 37-42.
[9] I. Chiarotto, M. Feroci, G. Sotgiu, A. Inesi, *Eur. J. Org. Chem.* **2013**, *2013*, 326-331.
[10] B. Gorodetsky, T. Ramnial, N. R. Branda, J. A. C. Clyburne, *Chem. Commun.* **2004**, *1*, 1972-1973.
[11] B. A. Rosen, S. Amin, M. R. Thorson, W. Zhu, D. T. Whipple, P. J. A. Kenis, R. I. Masel, *Science* **2011**, *334*, 643-644.
[12] A. Jena, H. Hsieh, S. Thoka, S. Hu, H. Chang, R. Liu, *ChemSusChem* **2020**, *13*, 2719-2725.
[13] D. Guan, X. Wang, M. Li, F. Li, L. Zheng, X. Huang, J. Xu, *Angew. Chem. Int. Ed.* **2020**, *59*, 19518-19524.
[14] Z. Li, M. Li, X. Wang, D. Guan, W. Liu, J. Xu, *J. Mater. Chem. A* **2020**, *8*, 14799-14806.
[15] Y. Xing, Y. Yang, D. Li, M. Luo, N. Chen, Y. Ye, J. Qian, L. Li, D. Yang, F. Wu, S. Guo, *Adv. Mater.* **2018**, *30*, 1803124.
[16] J. Zhou, X. Li, C. Yang, Y. Li, K. Guo, J. Cheng, D. Yuan, C. Song, J. Lu, B. Wang, *Adv. Mater.* **2018**, *31*, 1804439.
[17] C. Li, Z. Guo, B. Yang, Y. Liu, Y. Wang, Y. Xia, *Angew. Chem. Int. Ed.* **2017**, *129*, 9254-9258.
[18] C. Hu, L. Gong, Y. Xiao, Z. Xia, L. Ma, T. Wu, Y. Lin, J. Lu, K. Amine, L. Dai, *Adv. Mater.* **2020**, *32*, 1907436.
[19] H. Wang, K. Xie, Y. You, Q. Hou, K. Zhang, N. Li, W. Yu, K. P. Loh, *Adv. Energy Mater.* **2019**, *9*, 1901806.
[20] L. Qie, Y. Lin, J. W. Connell, J. Xu, L. Dai, *Angew. Chem. Int. Ed.* **2017**, *56*, 6970-6974.
[21] Y. Xiao, F. Du, C. Hu, Y. Ding, Z. L. Wang, A. Roy, L. Dai, *ACS Energy Lett.* **2020**, *5*, 916-921.

Author contributions

H. Peng and B. Wang directed the project. J. Li conceived the idea, carried out the experiments, analyzed the data, and wrote the original paper. K. Zhang assisted J. Li in simulation calculations, materials characterizations, and data analysis. C. Wang and L. Wang made material characterizations. All authors discussed the results and commented on the manuscript.